Single-Shot Optical Sectioning Using Two-Color Probes in HiLo Fluorescence Microscopy

Eleonora Muro,[†] Pierre Vermeulen,[†] Andriani Ioannou,[‡] Paris Skourides,[‡] Benoit Dubertret,[†] Alexandra Fragola,[†] and Vincent Loriette[†*]

[†]Laboratoire de Physique et d'Étude des Matériaux, Centre National de la Recherche Scientifique, UMR 8213, École Supérieure de Physique et de Chimie Industrielles, Paris, France; and [‡]Department of Biological Sciences, University of Cyprus, Nicosia, Cyprus

ABSTRACT   We describe a wide-field fluorescence microscope setup which combines HiLo microscopy technique with the use of a two-color fluorescent probe. It allows one-shot fluorescence optical sectioning of thick biological moving sample which is illuminated simultaneously with a flat and a structured pattern at two different wavelengths. Both homogenous and structured fluorescence images are spectrally separated at detection and combined similarly with the HiLo microscopy technique. We present optically sectioned full-field images of *Xenopus laevis* embryos acquired at 25 images/s frame rate.

INTRODUCTION

The ability to obtain optical sections of thick samples is mandatory for performing dynamic three-dimensional microscopy.

Apart from image deconvolution techniques, three different optical approaches are commonly used to obtain optical sections, or axial resolution:

The first is to limit the axial extent of illumination or detection, by localizing the excited or imaged volume. Stimulated emission depletion microscopy, second-harmonic generation, two-photon, and confocal microscopy (1) are examples of this approach in which the regions in the sample out of the limited illuminated volume do not participate in the image. Although most of those techniques allow us to build images at high frame rates, they are based on local sequential measurements and are thus sensitive to distortion caused by any movement of the sample during image acquisition.

The second approach is to add some structure, or information, to a wide-field illumination, and recover this information in the detected signal. Because the ability to reveal this information depends on the sample localization and spatial frequency content, optical sections can be obtained by clever data processing. A simple and efficient implementation of this concept is structured illumination microscopy (2) in which the in-focus content of an image is tagged with the image of a physical grid inserted in place of the illuminator field diaphragm. Structured illumination microscopy provides true axial resolution in the sense that all spatial frequencies in a sample, even the zero-frequency component, are attenuated by defocusing. Those wide-field approaches suffer from the same weakness as point-by-point techniques because, although all pixels in an image are recorded simultaneously, they require sequential partial measurements to build the final image, and are thus necessarily time-consuming and hardly compatible with the observation of dynamic events. In the case of structured illumination, for example, three images with different illumination patterns must be taken to extract one optical section. Single-image optical sectioning based on structured illumination has been obtained using a three-color pattern (3), or by polarization coding (4), but these setups are limited to the study of nonfluorescent or highly anisotropic samples.

The third approach is light-sheet microscopy, which allows us to selectively image a single plane with a wide-field microscope. Light-sheet microscopy has shown impressive capabilities at imaging through thick tissues (5), but strongly depends on the size and optical properties of the sample. Sample-induced aberrations widen the light sheet and generate background in the image. This technique is also restricted to transparent samples.

A step forward was made by Lim et al. (6), who introduced HiLo microscopy, in which only two en-face images, one of which uses speckle illumination, are sufficient to extract optical sections. With this approach, Lim et al. were able to perform full-field optical sectioning of moving samples (7). However, the two images required to build each optical section were recorded sequentially, one after the other. This makes the measurement sensitive to the sample movement. We propose an original implementation of Lim et al.'s approach to perform one-shot optical sectioning of fluorescent samples using two-color illumination and detection. The ability to use two illumination and two detection channels simultaneously allows us to record an image of the sample illuminated with a structured pattern and, at the same time, a second image taken with a uniform illumination.

This approach has two main advantages over those currently available: being a full-field approach, the time taken to build an optical section only depends on the integration time of the camera and not on the number of pixels, and

doi: 10.1016/j.bpj.2011.03.047

it is insensitive to spurious effects that may affect sequential measurement procedures such as those used by confocal or structured illumination microscopy. However, it must be emphasized that this two-color excitation and two-color emission setup is useless without the use of specific fluorescent probes having two well-separated absorption bands and two distinct emission bands.

MATERIALS AND METHODS

The HiLo image generation

HiLo microscopy aims at obtaining optical sections of thick samples, which means recovering the whole spatial frequency content of the in-focus part of the sample, though rejecting the out-of-focus low-frequency content of the whole sample, the out-of-focus high-frequency content being naturally eliminated by the low-pass imaging properties of the optical system. The principle of HiLo microscopy is described in Santos et al. (7) and Mertz and Kim (8). Our approach consists in obtaining optical sectioning by recording simultaneously two images of the sample—one with a uniform illumination; and one with structured illumination using two fluorescent probes, each sensitive to only one illumination. The in-focus low spatial frequency content is tagged by the structured illumination pattern, whereas the in-focus high-frequency content is present as the high-frequency content of the uniformly illuminated image. Various methods can be used to extract the full in-focus information and reject the out-of-focus blur, as emphasized in Mertz and Kim (8). In our particular setup, we face a difficulty which is not present when a single fluorescent probe species is used and one performs sequential image acquisition: we cannot suppose that the relative weight of in-focus and out-of-focus signals is the same in the two images. This extra difficulty led us to develop an adapted image-processing algorithm which is detailed in the Appendix.

Using our method, the in-focus image I_{if} is calculated by the formula

$$I_{if} = \frac{1}{\alpha_F}HF[I_F] + \frac{2}{\alpha_S''}\sqrt{(I_S\star O_S)^2+(I_S\star O_C)^2}, \qquad (1)$$

in which I_F is the uniformly illuminated image, I_S is the structured illumination image, HF is a high-pass filter, α_F and α_S'' are weights to be optimized, $\star$ denotes a convolution product, and O_S and O_C are the Gabor functions,

$$
\begin{aligned}
O_S(x,y;x_c,y_c) = {}& \sin\left(2\pi\frac{x-x_c}{p}\right)\\
& \times \exp\left(-K\frac{(x-x_c)^2+(y-y_c)^2}{p^2}\right),
\end{aligned}
\qquad (2)
$$

$$
\begin{aligned}
O_C(x,y;x_c,y_c) = {}& \cos\left(2\pi\frac{x-x_c}{p}\right)\\
& \times \exp\left(-K\frac{(x-x_c)^2+(y-y_c)^2}{p^2}\right),
\end{aligned}
\qquad (3)
$$

where p is the grid period in the image, and K is a scalar parameter to be optimized. A detailed description of the image calculation is presented in the Appendix. One important point to be mentioned here is the fact that the ratio of α_F and α_S'' must be constant across the image. This requires that the concentration ratio of the two fluorescent probes be the same everywhere in the sample and thus puts constraints on the way the probes are designed in the case of a staining with an exact localization (e.g., immunofluorescence labeling). To properly combine the two images for low-frequencies extraction, their relative lateral offset must be smaller than the grid period. In practice, a simple two-dimensional correlation is effective enough to obtain a residual offset of one pixel, much smaller than the grid period.

Optical setup

The optical setup presented in Fig. 1 is based on a commercial biological microscope body (model No. IX-71; Olympus, Melville, NY) equipped either with dry or water immersion objectives. Objectives characteristics are given later in Results and Discussion. Both illumination paths are used. The epi-illumination provides the structured illumination. The standard illuminator is modified by inserting a Ronchi grid (20 or 40 lines per millimeter; Edmund Optics, Barrington, NJ) in place of the field diaphragm. The grid does not move during acquisition so its holding can be made very simple, but a manual translation stage provides axial displacement to optimize the conjugation between the grid and the in-focus plane inside the sample, and a manual tip-tilt platform is used to orient the grid perpendicular to the microscope objective optical axis. This alignment step is performed by visual inspection of the grid image on a mirror and optimization of the grid contrast on the whole field of view. The trans-illumination provides the uniform illumination. Except for the lamp which is replaced by a laser, the upper illuminator remains unmodified.

A few extra optical components are used to adapt the laser beam shape to the illuminator input, and a rotating diffusing disk breaks the laser spatial coherence to provide speckle-free illumination. The two illuminations excite two different fluorescent probes. Both fluorescent signals travel through the same path out of the microscope, so a clever choice of the various filters and dichroic mirrors is a crucial issue for obtaining a good spectral separation of the two images simultaneously with a good rejection of the two illuminations. The overall excitation and emission filter transmission factors is given in Fig. 2.

Out of the microscope, the images are sent to an electron-multiplying charge-coupled device (CCD) (Cascade 512B 512 × 512 pixel camera; Roper Scientific, Trenton, NJ) through a channel-splitting optical setup that separates the two spectral components and directs them on different regions of a single camera. Each component is imaged on a 250 × 250 pixel region of the CCD array. This modest image size is not a limit of the setup, and only depends on the characteristics of the chosen camera. The main optical components are: two achromatic doublets; a dichroic mirror; two metal-coated mirrors; and two bandpass filters. The use of two mirrors on
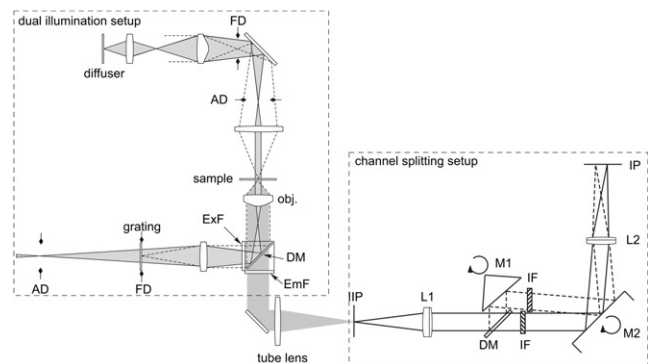

FIGURE 1 Optical setup. The dual illumination setup is based on a commercial microscope body and uses both the epi-illumination and trans-illumination paths. The channel-splitting setup is fixed on a camera output port. (*AD*, aperture diaphragms; *FD*, field diaphragms; *obj.*, microscope objective; *ExF*, excitation filter; *EmF*, emission filter; *DM*, dichroic mirrors; *IIP*, intermediate image plane; *L1* and *L2*, achromats; *M1* and *M2*, silver-coated mirrors, *IF*, interference filters; and *IP*, camera image plane.) The light sources are not represented.
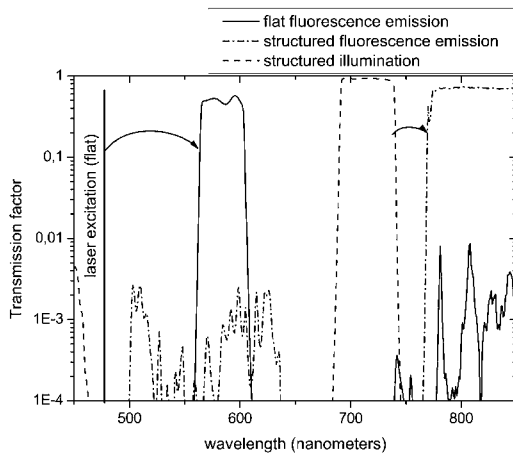
FIGURE 2   Excitation and emission filters transmission factors. A good separation of the excitation bands is required to avoid unwanted structured illumination of the otherwise homogeneously illuminated probes, and a good separation of the emission bands is necessary to limit the presence of spurious structured signal in the flat illumination image. The structured illumination filter set is composed of FF01-716/43, Q500LP bandpass filters followed by a reflection on a Q750LP dichroic filter; the structured emission path is composed of a transmission by Q750LP followed by transmissions by TE500LP, TFF740 (dichroic), and T810/90. The uniform emission path is made of transmission by Q750LP and TE500LP, reflection on TFF740, and transmission by THQ585/40. All filters are from Chroma Technology (Bellows Falls, VT), except the TFF740 and FF01-716/43, which are made by Semrock (Rochester, NY).

tip-tilt platforms allows a fine adjustment of both the separation of the two subimages and their position on the camera. As can be seen in Fig. 1, the two optical paths are not equal, and in practice, they differ by a few centimeters.

To have the two images record the sample object plane, it is necessary to optimize the positions of both lenses. The camera must be placed on the second lens image plane while the intermediate image plane at the output of the microscope must be placed on the first lens object plane. This step is performed by standard autocollimation methods, before the optical system is placed behind the microscope. An iris diaphragm is placed on the intermediate image plane to limit the size of the images and avoid the superposition of the subimages on the camera. The presence of the two lenses between the intermediate image plane and the camera allows us to add an optional magnification or reduction factor. For practical reasons we decided to use a ×1.5 magnification. After taking into account the extra magnification, the maximum field-of-view diameter that can be imaged on separate subimages on the camera is 2.35 mm/G where G is the objective magnification. The grid period p on the CCD camera does not depend on the objective magnification, and in our setup is equal to $p = 9.43$ pixels when using a 20-lines/mm grid.

Two-color fluorescent bead preparation

The two-color probe we designed for specific staining of fluorescent beads (see Fig. 3) is composed of home-made quantum dots (emission peak at 575 nm) and Alexa 750 (emission peak at 776 nm) (Invitrogen, Carlsbad, CA). We linked the two fluorophores together to have a constant signal ratio for the two channels across the beads (Figs. 4 and 5). We introduced a rigid spacer with a controlled length to reduce as much as possible the Förster resonance energy transfer (FRET) between the two fluorophores while keeping them close together. This is a very flexible solution because the spacer is an oligonucleotide which size can be adapted depending on the

couple of fluorophores to be used. We can calculate the FRET efficiency depending on the distance between the two fluorophores and introduce a number of basepair in the DNA spacer accordingly (knowing that one nucleotide unit is ~3.3 Å). We define the FRET efficiency E as in Mattoussi and Cheon (9)

$$E = \frac{\rho}{\rho + \left(\dfrac{r}{R_0}\right)^6},\qquad(4)$$

where r is the donor/acceptor distance, R_0 is the Förster distance, and ρ is the acceptor/donor ratio. The Förster distance is given by

$$R_0^6 = \frac{9Q_0 \ln(10)\kappa^2 J}{128\pi^5 n^4 \mathcal{N}_A},\qquad(5)$$

where Q_0 is the quantum yield of the donor in the absence of acceptor, κ is the dipole orientation factor, n is the medium index of refraction, and $\mathcal{N}_A$ is Avogadro's number. The spectral overlap J is calculated by

$$J = \int f_D(\lambda)\epsilon_A(\lambda)\lambda^4 d\lambda,\qquad(6)$$

with f_D the normalized donor emission spectrum, and ε_A the acceptor molar extinction coefficient. For the two fluorophores, we evaluated experimentally $R_0 = 50$ Å, and in the predicted case of $\rho = 4$ (QD: Alexa ratio = 1:4), then $E = 5\%$ at $r = 80$ Å. We use a DNA spacer of 15 bp, which corresponds to a 50 Å length. The QD radius is 33 Å and the presence of surface ligands and streptavidin on the QD increase the QD/Alexa distance by 30 Å, so in our case $R = 113$ Å and FRET should be negligible (<0.2%). We choose QDs because they possess a very narrow emission spectrum, so the FRET is further reduced; but an organic fluorophore could be used as well, because we took in consideration the possibility of a low FRET-derived signal.

In our instrumental layout, the uniform illumination channel fluorophore is the donor. Therefore, if a FRET-derived signal is generated, it will pollute the structured illumination channel (the acceptor channel), which will decrease the grid contrast. If the grid contrast stays higher than 0.1, the reconstructed image will not be significantly affected by FRET, as can be seen in Fig. 3 B. If the opposite configuration were used (the donor on the structured channel) the reconstructed image could contain artifacts in the form of a spurious grid pattern because the uniform illumination channel would also contain structured information.

QDs-Streptavidin (SA) were prepared as described in Muro et al. (10): 0.25 nmol of QDs-SA were incubated with 10 equivalents of the oligonucleotide 1-biotin and left to react for 30 min. The presence of the oligonucleotide 1 on QDs was verified by incubation with oligonucleotide 2 (the complementary strand of oligonucleotide 1) containing beads. The ratio between QDs-SA and the oligonucleotide allowed a partial saturation of Streptavidin-binding sites, which was verified by a significant decrease of the affinity for biotin agarose beads. Streptavidin-Alexa750 was obtained mixing 50 equivalent of Alexa 750 succinimidyl ester (Invitrogen) with Streptavidin (BIO SPA, Milan, Italy).

The purification was performed with NAP5 Sephadex G-25 (GE Healthcare Life Sciences, Piscataway, NJ) and ultrafiltration columns. SA-Alexa750 was then incubated with an equivalent amount of the oligonucleotide 2-biotin and left to react for 30 min. The presence of the oligonucleotide 2 on SA-Alexa750 was verified by incubation with oligonucleotide 1 containing beads. The two complexes then were placed in HEPES 0.1 M, pH 7.4, 200 mM NaCl, 200 mM CaCl$_2$ by ultrafiltration, incubated 10 min at 37°C, and stirred overnight to allow the basepairing of the two strands. The purification was performed by ultracentrifugation and the migrated band was collected. The absorption spectra of the migrated band revealed that the final ratio QDs: SA/Alexa was 1:1. We estimated that SA/Alexa is ~1:4. The complex QD-Alexa was then incubated for 15 min with biotin beads, washed three times, and imaged.
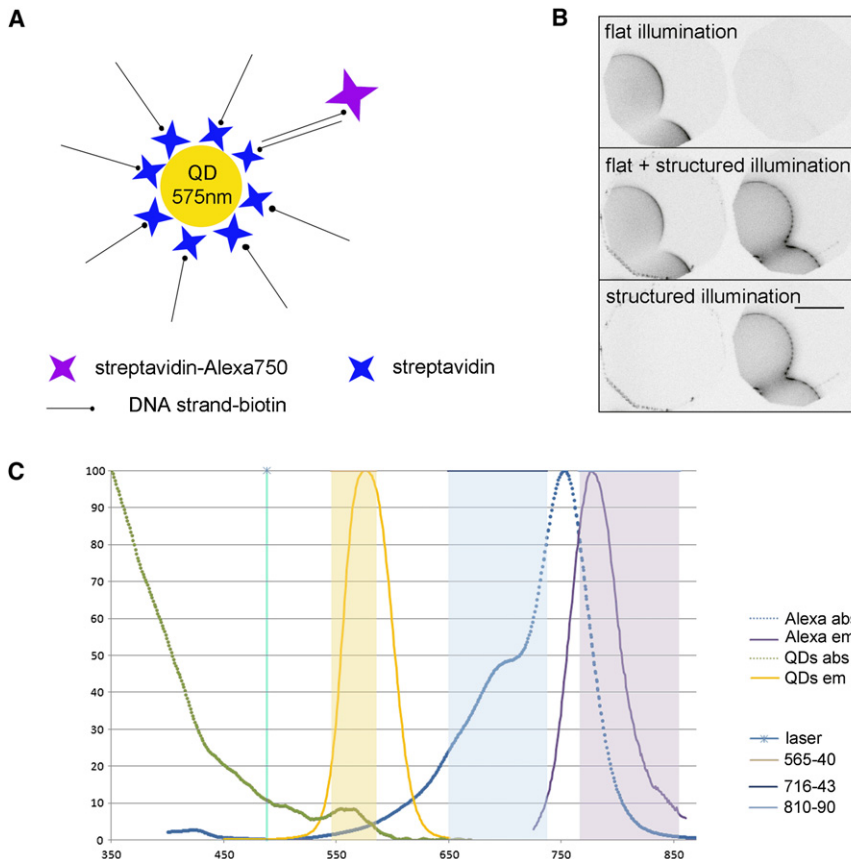
FIGURE 3 (*A*) Scheme of the probe design. (*B*) Images of fluorescent spheres acquired with the uniform illumination channel only, the structured illumination channel only, and both. Note there is no signal in the right part of the upper image (when only the acceptor is irradiated), which proves that there is no apparent generation of FRET. (*C*) Emission and absorbance spectra of quantum dots and Alexa.

Two-color fluorescent *Xenopus laevis* embryo preparation

Xenopus laevis embryos from induced spawning (11) were staged according to Nieuwkoop and Faber (12). Operation techniques and Marc's Modified Ringer's (MMR) buffer have been described in Winklbauer (11). *Xenopus* embryos were fertilized in vitro and dejellied using 2% cysteine-HCl, pH 7.8, then maintained in 0.1 × MMR. Microinjections were performed in 4% Ficoll in 0.33 × MMR. The embryos were injected with Alexa Fluor 750 nm (Invitrogen) near-infrared fluorophore and 575-nm emitting bidentate zwitterionic dihydrolipoic acid-sulfobetaine QDs (10) at the four-cell stage according to established protocols (13). For that sample, the Alexa and the QDs do not need to be linked, because once introduced via microinjection to one cell at the animal pole, cell divisions gave rise to a progeny of cells all containing both fluorophores in contrast to neighboring cells which have neither fluorophore.
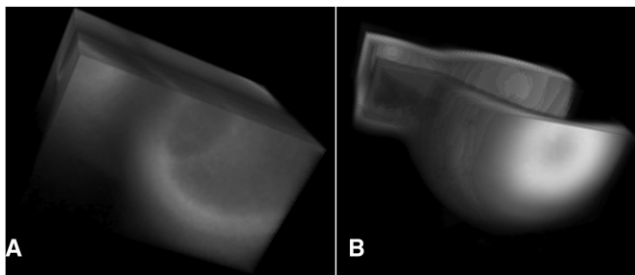

FIGURE 4 Three-dimensional HiLo image of fluorescent beads in three dimensions, images using a 20 lines/mm grid and a ×20 objective. (*A*) Raw volume. (*B*) HiLo volume.

Colocalization refers to the localization of the fluorophores within the same cells rather than intracellular compartments which are invisible at this low magnification. The embryos were allowed to develop to blastula stage (stage 6.5–7) and were then fixed in 1× MEMFA for 2 h at room temperature, dehydrated in methanol, and stored for subsequent imaging. Clearing of embryos was carried out by immersion in two parts benzyl benzoate and one part benzyl alcohol (BB/BA) after dehydration in methanol. The refractive index of BB/BA closely matches the refractive index of yolk, thereby rendering *Xenopus* embryos nearly transparent.

Optical system performances

The optical sectioning performances were tested by imaging either a mirror or a thin continuous fluorescent plane. Although the image reconstruction is not a linear operation and cannot be simply represented by an optical transfer function, the optical sectioning properties of a structured illumination system can be described by a function which is formally identical to the optical transfer function of a conventional microscope (14). In the fluorescent case, the excitation wavelength differs significantly from the emission wavelength, so the microscope equivalent optical transfer function G from the field diaphragm to the detector can be written as the product of two distinct functions. The first characterizes the optical system from the grid to the sample and the second from the sample to the detector, as

$$G(\nu, z) = C(\nu_{exc}, z)C(\nu_{em}, z), \tag{7}$$

where

$$\nu_{exc} = p^{-1}\lambda_{exc}/NA \text{ and } \nu_{em} = p^{-1}\lambda_{em}/NA$$

are reduced spatial frequencies, λ_{exc} and λ_{em} are the excitation and emission wavelengths in vacuum, NA is the objective numerical aperture, z is the
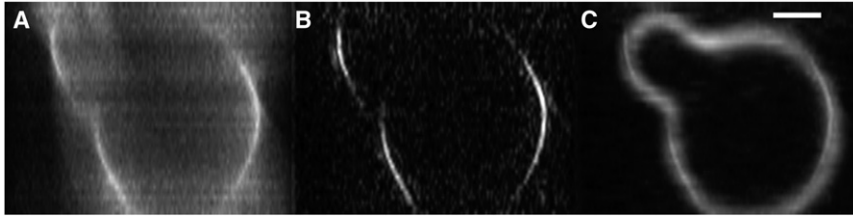
FIGURE 5 *X-Z* Two-dimensional sections of a three-dimensional image of fluorescent beads. (*A*) Standard fluorescent image. (*B*) Standard fluorescent image, high-pass-filtered. (*C*) HiLo image. The images were not processed except image *B*, for which the contrast was enhanced. The scale bar is 20-μm long.

defocus, and *p* is the grid period in the sample. An approximate solution for the individual functions *C* is found in the obligatory Stokseth article (15),

$$C(\nu,z) \;=\; 2f(\nu)\frac{J_1\left(\frac{8\pi}{\lambda}nz\sin^2\left(\frac{\alpha}{2}\right)\nu\left(1-\frac{\nu}{2}\right)\right)}{\left(\frac{8\pi}{\lambda}nz\sin^2\left(\frac{\alpha}{2}\right)\nu\left(1-\frac{\nu}{2}\right)\right)}, \quad (8)$$

where *n* is the immersion medium index of refraction, λ is either the emission or excitation wavelength, α is the objective half-aperture angle, and *f* is the function

$$f(\nu) \;=\; 1 - 0.69\nu + 0.0076\nu^2 + 0.043\nu^3. \quad (9)$$

In the case where the sample is a mirror, the excitation and emission wavelengths are equal and the mirror reflects the incident field, so the equivalent optical transfer function is given by (14)

$$G(\nu,z) \;=\; C(\nu_{exc},2z). \quad (10)$$

Table 1 summarizes the theoretical full width at half-maximum of optical section signals for different microscope objectives and different grid periods. We used water immersion $\times 20$ NA = 0.7 (UAPO/340; Olympus) $\times 60$ NA = 1.2 (UPlanSAPO; Olympus) and a $\times 10$ NA = 0.3 dry objective. In the calculations, we took into account the fact that the magnification factor from the field diaphragm to the sample differs from the nominal magnification factor, by a factor one-half in our particular setup. For the fluorescent case, we took $\lambda_{exc} = 450$ nm and $\lambda_{em} = 565$ nm, and for the mirror case, we took $\lambda = 810$ nm. To perform the measurements with the mirror, we had to modify the illumination setup so that both flat and structured illuminations were coming from the same side. The sometimes large discrepancy between theoretical and measured values, particularly when using the $\times 60$ NA = 1.2 objective with the fluorescent sample, has different sources. The main one is the sensitivity to the coverglass thickness.

We measured, using a mirror sample and the $\times 60$ objective, that the optical sectioning strength is degraded by a factor 1.7 if the cover-glass thickness differs by $\pm 15\%$ from its nominal value, a dispersion commonly observed in cover-glass batches. A second source is the finite thickness of the fluorescent plane which enlarges the experimental sections thickness. Lastly, the excitation and emission pupils are, in practice, different. The field diaphragm in our particular epi-illumination setup produces vignetting of the aperture diaphragm image on the objective back-focal plane, so the apparent illumination numerical aperture is slightly reduced compared to the objective numerical aperture. The image path in the fluorescent case, on the contrary, uses the full objective numerical aperture.

The ability to recover all spatial frequencies from three-dimensional objects is clearly apparent when looking at coated hollow spheres. Optical sections of spheres have a spatial frequency content that varies with depth: low frequencies make the top and bottom, whereas high frequencies are dominant in the equatorial zone. Two-color HiLo images of spheres are presented in Fig. 4. The HiLo images shown, as well as the images presented in Results and Discussion, have been built using the algorithm presented in the annex; they have not been filtered, enhanced, nor thresholded afterwards. They are presented in a linear gray-shaded palette. For comparison, transverse cuts of the volume are compared with high-pass-filtered standard images and raw standard images in Fig. 5. HiLo allows a complete reconstruction of the spheres, although high-pass and standard images miss the upper and lower parts of the spheres. The whole volume was built from 30 sections and four images per section. The complete measurement time, comprising the exposure periods and the piezo axial displacement time, was 40 s.

RESULTS AND DISCUSSION

We used our two-color HiLo microscope to realize fluorescence sectioning of thick biological samples. *Xenopus laevis* embryos were injected with both 575-nm emitting quantum dots and Alexa 750 as described in Materials and Methods. Both Alexa 750 and QDs fluorescence levels and concentrations remain homogeneous and stable in the embryo cells even after numerous divisions. Because the colocalization of these two necessary wavelengths was preserved, the fluorophores were injected without any DNA-spacer between them. Embryos were clarified before imaging using the protocol described in Materials and Methods, to minimize light scattering and enhance the contrast of the grid projection into the sample.

The whole embryo was ~1 mm in diameter, and was first observed in full-field classical fluorescence microscopy with a $\times 5$ NA = 0.15 dry objective (MPlanFLN; Olympus) (Fig. 6 *A*): cells at the surface could be observed with a high background fluorescence signal coming from the out-of-focus planes of this thick sample, and the spherical shape of the embryo acted like a ball lens and created a strong artifact as a bright ring surrounding it.
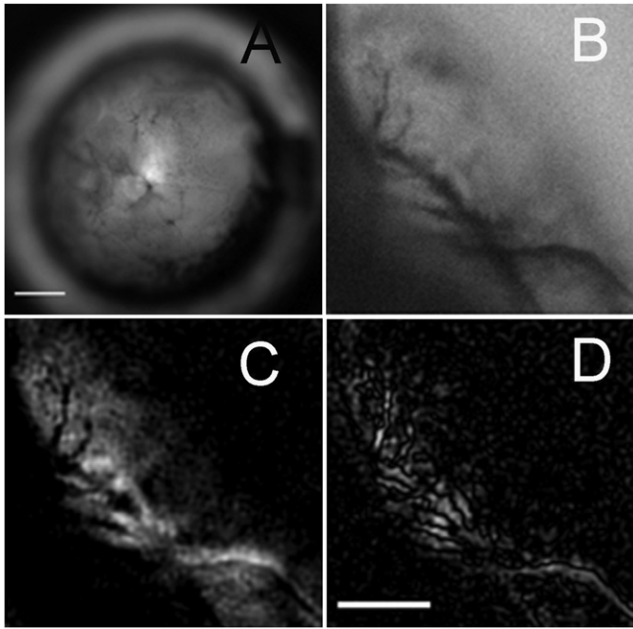
TABLE 1 Calculated (and measured) thickness in micrometers of the optical sections for different objectives and grids, with a fluorescent sample and a nonfluorescent reflecting surface

Grid lines/mm	$\times 60$, NA = 1.2		$\times 10$, NA = 0.3		$\times 20$, NA = 0.7	
	Fluorescence	Mirror	Fluorescence	Mirror	Fluorescence	Mirror
20	0.78 (2.83)	0.58 (0.77)	18.6 (23.9)	12.8 (20.0)		
40	0.46 (1.83)	0.39 (0.88)			2.6 (4.37)	2.0 (3.4)

For the fluorescent case, $\lambda_{exc} = 450$ nm and $\lambda_{em} = 565$ nm, and for the mirror case, we took $\lambda = 810$ nm.

FIGURE 6 Whole *Xenopus laevis* embryo imaged in a standard epi-fluorescence microscope (*A*), standard (*B*), HiLo (*C*), and high-pass-filtered standard images (*D*) of a region of the whole embryo. A 50-μm scale bar is shown in image *A*, and panels *B–D* have a 50-μm scale bar. The high-pass-filtered image contains negative values. The lookup table ranges linearly from minimum (negative) to maximum (positive) value.

Even after clarification, scattering in the embryo is still important and does not allow us to maintain a good grid contrast when imaging inside the sample. We were thus only able to improve the image quality of peripheral cells. Nevertheless, two-color HiLo microscopy brings an improvement by rejecting the out-of-focus fluorescence signal that degrades the image contrast and thus can hide details in the in-focus plane. We acquired two-color HiLo images using a ×20 NA = 0.5 objective (UPlanFLN; Olympus) objective and a 20-lines/mm grid. When using this objective, the thickness of the optical sections is approximately equal to 40 μm.

Fig. 6 shows the classical fluorescence image (Fig. 6 *B*) and the two-color HiLo image (Fig. 6 *C*) of the same area of the embryo and clearly demonstrates that the two-color HiLo technique efficiently removes the background fluorescence signal and reveals the in-focus plane information. Fig. 6 *D* presents the corresponding high-pass-filtered image and confirms the gain of the HiLo technique in optical sectioning by preserving both high and low frequencies of the in-focus plane. Fig. 7 was acquired with the ×5 NA = 0.15 objective and the same 20-lines/mm grid. It shows a detail of the embryo and also demonstrates the gain of two-color HiLo microscopy (Fig. 7 *B*) compared to classical fluorescence microscopy (Fig. 7 *A*). The spurious bright ring around the sample is suppressed, whereas fluorescent cells of the embryo are imaged with an enhanced contrast. This is confirmed by comparing the same profile in the two
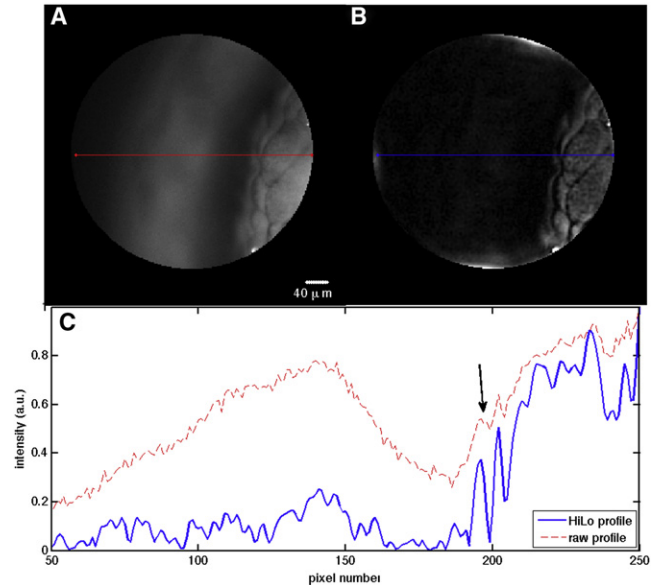

FIGURE 7 Raw (*A*) and HiLo (*B*) images of a peripheral region of a *Xenopus laevis* embryo shown in Fig 6. (*C*) Two profiles corresponding to the two colored lines in panels *A* and *B*.

images (Fig. 7 *C*). The signal coming from the artifact is removed, leading to a quite flat background; the out-of-focus fluorescence signal is also removed, allowing us to reveal details of the in-focus plane (like around pixel 200, marked by a *solid arrow*).

The interest of HiLo microscopy leads in discriminating the low spatial frequency information of the in-focus plane from out-of-focus regions. The gain of using such a microscope therefore depends on the spatial spectrum of the sample. If the size of the structure to be revealed is smaller than the period of the image of the grid into the sample, a simple high-pass filter should remove the background made of fluorescence of the out-of-focus planes. HiLo microscopy is useful when we need to observe, into a deep sample, continuous or slowly varying structures whose characteristic spatial extent is greater than the grid period.

The efficiency of the two-color HiLo microscope strongly depends on the spatial colocalization of the two wavelengths used for the homogeneous and the structured images. If there is a lack of one of the fluorophores in a sample area, the division of the structured image by the flat one would generate artifacts. As we showed in this article, depending on the nature of the sample, we can just inject a mixed solution of the two fluorophores into it or it can be necessary to link them before introduction. When the two fluorophores have to be confined in a restricted region of interest in the sample (as in the case of specific labeling), we have to link them together to obtain an exact colocalization and to reduce FRET.

When a region of the sample much larger than the observed region can be uniformly stained (as in the case of cellular lineage in embryos), the linkage is unnecessary

to obtain an exact colocalization and the distance between them should be globally higher than the Forster radius. Note that the variation of fluorescence intensity due to photobleaching during acquisition is not a problem as long as the fluorescence can be measured and the photobleaching is spatially homogeneous. High and low frequencies, which respectively correspond to orange and infrared colors, are summed with arbitrary coefficients that can be adjusted (see Eq. 18). Artifacts in the HiLo image intensity can appear if photobleaching is not homogeneous in the structured image; for example, if some stained areas move during the acquisition time while other regions stay fixed. In this case, the local grid contrast will depend on the local sample speed. However, this artifact does not degrade the optical sectioning properties of the system.

The main advantage of performing simultaneous acquisition of both structured and flat images on a single CCD chip is the ability to obtain optical sections of moving samples. The frame rate is limited by the camera-frame transfer speed and the integration time by the signal/noise in the structured illumination image. The use of a coherent source may generate speckle that could show up in the images at high frame rates or short integration times. In our particular setup, we use a one-inch radius diffusing-disk rotating at 5 rps, illuminated by a 2-mm diameter laser spot. This effect becomes visible for integration times shorter than 4 ms. This limit can be easily overcome by increasing the speed of the rotating disk. It is important to note that the time taken to obtain an optical section does not depend on the image size.

Fig. 8 shows five images of a moving embryo taken with a ×5 objective. The camera was running with an integration time of 10 ms at 25 frames/s. Speed of the embryo was ~220 μm/s. The embryo moved by 2.2 μm during the exposure time of a single image and 9 μm between two images. The sample movement blurs the high spatial frequency content of the sample, but does not degrade the ability to recover the in-focus low-frequency content as long as the sample movement is smaller than one illumination period during the CCD integration time.

CONCLUSIONS

The implementation of HiLo microscopy that we propose allows full-field optical sectioning in only one image acquisition. This permits us to increase the acquisition speed, which is critical for imaging of dynamic objects, up to the camera frame rate. Additionally, because the two images required for the reconstruction are collected in a single shot, the displacement of the object does not induce reconstruction artifacts, but only a reduction of the spatial bandwidth in the reconstructed image. Moreover, the setup is, by design, insensitive to FRET. We present full-field optical sections of moving samples taken with an integration time of 10 ms and a frame rate of 25 frames/s. The results pre-
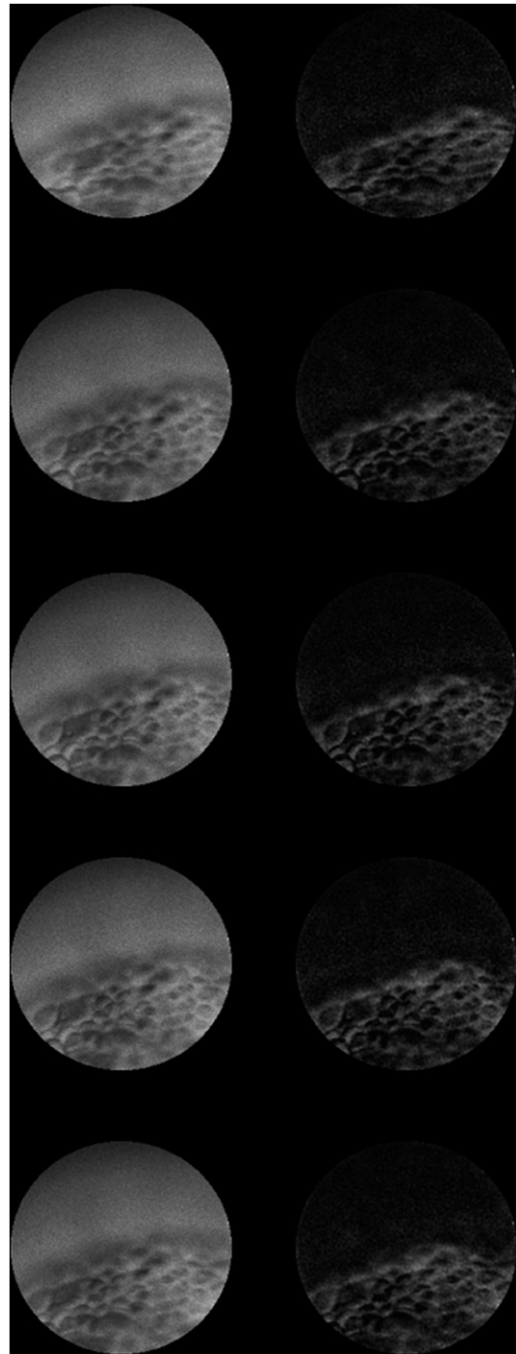

FIGURE 8 Sequence of five consecutive images of a moving sample recorded at 25 frames/s. The time of integration is 10 ms and the apparent field diameter is 450 μm. (*Upper row*) Images taken with the flat illumination. (*Lower row*) HiLo processed images.

sented are acquired at rates which are only limited by the emitter brightness and the camera sensitivity and speed.

The system is implemented on a commercial microscope body and preserves all its original performances and capabilities. It does not require complex setup or alignment procedures or image processing.

APPENDIX

The method we adopt to recover the optical section image is largely inspired from Santos et al. (7). However the use of two different fluorescent species ands two distinct illumination setups requires extra image processing steps that eventually lead to Eq. 1.

The in-focus content of an image is denoted I_{if} and the out-of-focus background is denoted I_{of}. The image recorded with a flat illumination is noted I_F and written as a linear combination of the two subimages

$$I_F = \alpha_F I_{if} + \beta_F I_{of}, \qquad (11)$$

where α_F and β_F are the weights of the two subimages. The structured illumination is characterized by a period p and a contrast C. The structured illumination image I_S is written as

$$I_S = \alpha_S \frac{1 + C \sin\left(2\pi\frac{x}{p}\right)}{1 + C} I_{if} + \beta_S I_{of}, \qquad (12)$$

that can be recast as

$$I_S = \left[\alpha_S' + \alpha_S'' \sin\left(2\pi\frac{x}{p}\right)\right] I_{if} + \beta_S I_{of}. \qquad (13)$$

In the single side-band extraction scheme presented in Santos et al. (7), one computes the ratio of the two images

$$D = \frac{I_S}{I_F} = \frac{\alpha_S' I_{if} + \beta_S I_{of}}{\alpha_F I_{if} + \beta_F I_{of}} + \sin\left(2\pi\frac{x}{p}\right)\frac{\alpha_S'' I_{if}}{\alpha_F I_{if} + \beta_F I_{of}}, \quad (14)$$

and Fourier-transforms the result

$$\mathcal{F}(D) = \mathcal{F}\left(\frac{\alpha_S' I_{if} + \beta_S I_{of}}{\alpha_F I_{if} + \beta_F I_{of}}\right) + \sqrt{\frac{\pi}{2}}\left[\delta\left(k - k_p\right)\right.$$
$$\left. - \delta\left(k + k_p\right)\right] \star \mathcal{F}\left(\frac{\alpha_S'' I_{if}}{\alpha_F I_{if} + \beta_F I_{of}}\right), \qquad (15)$$

where $\star$ denotes a convolution. The Fourier transform of D contains three parts. The first Fourier-transform is centered around the zero spatial frequency $k = 0$, whereas two other components are shifted by $k_p = 2\pi/p$. One can isolate any of the two shifted spectra by bandpass filtering $\mathcal{F}(D)$,

$$BP[\mathcal{F}(D)] = \sqrt{\frac{\pi}{2}}\delta\left(k - k_p\right) \star \mathcal{F}\left(\frac{\alpha_S'' I_{if}}{\alpha_F I_{if} + \beta_F I_{of}}\right)$$
$$= \sqrt{\frac{\pi}{2}}\delta\left(k - k_p\right) \star \mathcal{F}\left(\frac{\alpha_S'' I_{if}}{I_F}\right), \qquad (16)$$

so that

$$I_{if,low} = \left\| \sqrt{\frac{2 I_F}{\pi \alpha_S''}} \mathcal{F}^{-1}\{BP[\mathcal{F}(D)]\} \right\|. \qquad (17)$$

Thus, by bandpass filtering, one is able to recover the in-focus content within the filter bandpass. The frequency content outside of this bandpass

is obtained by high-frequency filtering I_F: because the high frequencies are only present in I_{if}, then

$$HF[I_F] = HF\left[\alpha_F I_{if}\right] = \alpha_F I_{if,high}.$$

The final in-focus image is computed by a weighted sum of the two components:

$$I_{if} = \frac{1}{\alpha_F} HF[I_F] + \left\| \sqrt{\frac{2 I_F}{\pi \alpha_S''}} \mathcal{F}^{-1}\{BP[\mathcal{F}(D)]\} \right\|. \qquad (18)$$

This approach works well as long as

$$\alpha_S'/\beta_S = \alpha_F/\beta_F,$$

because in this case the central spectrum reduces to a Dirac δ. This is only the case if the relative weight of in-focus and out-of-focus signals is the same in the two images. In our setup, this requirement is not necessarily fulfilled. The main problem is then that the centered spectrum

$$\mathcal{F}\left(\frac{\alpha_S' I_{if} + \beta_S I_{of}}{\alpha_F I_{if} + \beta_F I_{of}}\right) \qquad (19)$$

usually spans far in the frequency domain, farther than k_p and thus superimposes with the shifted spectra within the bandpass filter band:

$$BP\left[\mathcal{F}\left(\frac{\alpha_S' I_{if} + \beta_S I_{of}}{\alpha_F I_{if} + \beta_F I_{of}}\right)\right] \neq 0. \qquad (20)$$

This introduces strong artifacts in the extraction of I_{if}. One way to get rid of this is by preprocessing I_S so that it contains only the modulated part

$$\alpha_S'' \sin\left(2\pi\frac{x}{p} + \phi\right) I_{if}.$$

One way to do that is to convolve I_S by a suitable convolution kernel. One possibility is to use a Gabor function

$$O_S(x, y; x_c, y_c) = \sin\left(2\pi\frac{x - x_c}{p}\right)$$
$$\times \exp\left(-K\frac{(x - x_c)^2 + (y - y_c)^2}{p^2}\right), \qquad (21)$$

where (x_c, y_c) values are the central coordinates of the kernel and K is a scalar value to be optimized. At each point (x_c, y_c), I_S is replaced by

$$I_S'(x_c, y_c) = \iint I_S(x, y) OS(x, y; x_c, y_c) dx dy. \qquad (22)$$

Because the integral of the convolution kernel vanishes, only the sine-modulated part of I_S gives a significant contribution to this integral, so that

$$I_S'(x_c, y_c) \approx \alpha_S'' \iint \sin\left(2\pi\frac{x}{p}\right) \sin\left(2\pi\frac{x - x_c}{p}\right)$$
$$\times \exp\left(-K\frac{(x - x_c)^2 + (y - y_c)^2}{p^2}\right) I_{if} dx dy, \qquad (23)$$

$$I_S'(x_c, y_c) \approx \frac{\alpha_S''}{2}\left[\cos\left(2\pi\frac{x_c}{p}\right) \iint \exp\left(-K\frac{(x - x_c)^2 + (y - y_c)^2}{p^2}\right) I_{if} dx dy\right.$$
$$\left. + \iint \cos\left(2\pi\frac{2x - x_c}{p}\right) \exp\left(-K\frac{(x - x_c)^2 + (y - y_c)^2}{p^2}\right) I_i dx dy\right]. \qquad (24)$$
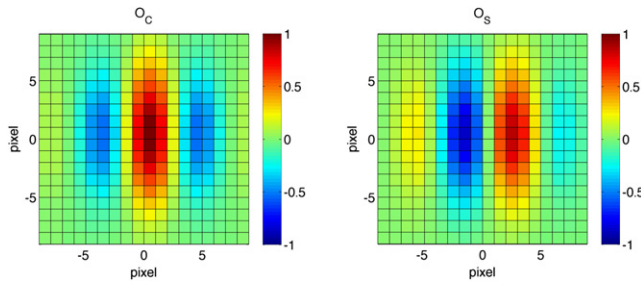
FIGURE 9 Convolution kernels OC and OS sampled on a 19×19 pixel grid. The period of the harmonic part is $p = 9.43$ pixels.

The integrals are evaluated numerically over a finite domain, the Gabor functions being computed on inside a $2p \times 2p$ square surface. The second integral calculated over this finite domain gives a negligible contribution

$$\frac{\iint \cos\left(4\pi\frac{x}{p}\right) \exp\left(-K\frac{x^2}{p^2}\right)dx}{\iint \exp\left(-K\frac{x^2}{p^2}\right)dx} < 3 \times 10^{-3}, \qquad (25)$$

for $0.4 < K$. If I_{if} is relatively smooth, and does not exhibit strong features like a very narrow spectral content, the second integral is usually negligible compared to the first. Noting that the first integral is simply a low-pass filter (convolution with a Gaussian function in the spatial domain), one may write

$$I'_S(x_c, y_c) = \frac{1}{2}\alpha''_S \cos\left(2\pi\frac{x_c}{p}\right)LP\left[I_{if}\right](x_c, y_c), \qquad (26)$$

where the low-pass cutoff frequency depends on the choice of K. We end with

$$\mathcal{F}(D) = \sqrt{\frac{\pi}{2}}\left[\delta\left(k - k_p\right) + \delta\left(k + k_p\right)\right] \star \mathcal{F}\left(\frac{\frac{1}{2}\alpha''_S LP\left[I_{if}\right]}{\alpha_F I_{if} + \beta_F I_{of}}\right), \qquad (27)$$

and do not have the centered spectrum problem anymore, and the shifted spectra are low-pass-filtered. The remaining steps of the calculation are identical to the one previously described.

Direct low-frequency extraction

The in-focus low-frequency content of the structured image I_S can also be recovered by measuring the local amplitude of the projected sine pattern. If one uses a second convolution kernel with its harmonic part phase shifted by $\pi/2$, as

$$\begin{aligned} O_C(x, y; x_c, y_c) &= \cos\left(2\pi\frac{x - x_c}{p}\right) \\ &\quad \times \exp\left(-K\frac{(x - x_c)^2 + (y - y_c)^2}{p^2}\right), \end{aligned} \qquad (28)$$

and performs the same convolution (with the same approximations), the result is

$$I''_S(x_c, y_c) = \frac{1}{2}\alpha''_S \sin\left(2\pi\frac{x_c}{p}\right)LP\left[I_{if}\right](x_c, y_c), \qquad (29)$$
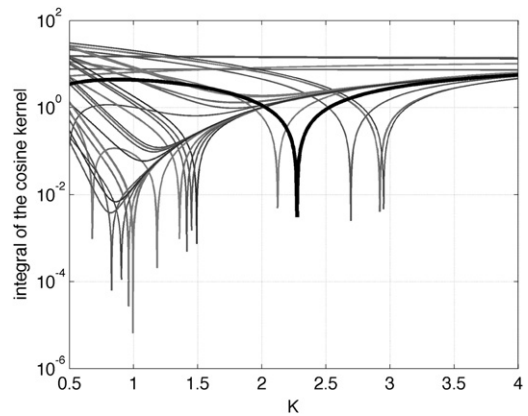
FIGURE 10 $\iint O_C(x, y)dxdy$, $p = 4.63$ pixels, as a function of K for different surfaces of integration ranging between 3×3 and 61×61 pixels. (*Solid plot*) Calculated with a 19×19 pixels' surface of integration.

so that

$$LP\left[I_{if}\right] = \frac{2}{\alpha''_S}\sqrt{(I_S \star O_S)^2 + (I_S \star O_C)^2}, \qquad (30)$$

and we obtain the in-focus low-frequency content directly without Fourier transform. Equation 30 is inserted into Eq. 18 in place of the low-frequency part to give Eq. 1. The cutoff frequency depends on the value of K in the kernels definitions. The higher the value of K, the thinner the low-pass filter. If one wants a low-pass that cuts at half the modulation frequency, then $K = 1$. However, the choice of K is not free. For a given size of the convolution, kernels support, and a given sampling interval, only one value of K will, at the same time, make the spurious term in Eq. 24 negligible and the integral of the convolution kernel vanish.

For example, if one modulation period is sampled over 9.43 pixels and the kernels are calculated on a 19×19 pixels surface, then $K = 2.27$; and $K = 1.36$ if one uses a 37×37 pixels surface. Fig. 9 is a representation of the O_C and O_S functions on a 19×19 pixels surface with $K = 2.27$. Fig. 10 shows calculated values of the integral of the cosine kernel as a function of the K parameter for different values of the surface of integration. For a given surface, at most one value of K makes the integral vanish, and this also fixes the low-pass properties of the kernel. In some cases, no value of K can be found that makes the integral vanish. The best value for K also depends on the spatial frequency content of the sample and on the image signal/noise because the spurious term in Eq. 24 also depends on the image characteristics. The optimization of K is ultimately performed based on subjective considerations. Visually, one obtain good results with K between two and three.

REFERENCES

1. Gustafsson, M. G. L. 1999. Extended resolution fluorescence microscopy. *Curr. Opin. Struct. Biol.* 9:627–634. (And references therein).

2. Karadaglić, D., and T. Wilson. 2008. Image formation in structured illumination wide-field fluorescence microscopy. *Micron.* 39:808–818.

3. Krzewina, L. G., and M. K. Kim. 2006. Single-exposure optical sectioning by color structured illumination microscopy. *Optics Lett.* 31:47–479.

4. Wicker, K., and R. Heintzmann. 2010. Single-shot optical sectioning using polarization-coded structured illumination. *J. Opt.* 12:084010.

5. Santi, P. A., S. B. Johnson, …, J. R. Leger. 2009. Thin-sheet laser imaging microscopy for optical sectioning of thick tissues. *Biotechniques.* 46:287–294.

6. Lim, D., K. K. Chu, and J. Mertz. 2008. Wide-field fluorescence sectioning with hybrid speckle and uniform-illumination microscopy. *Opt. Lett.* 33:1819–1821.

7. Santos, S., K. K. Chu, …, J. Mertz. 2009. Optically sectioned fluorescence endomicroscopy with hybrid-illumination imaging through a flexible fiber bundle. *J. Biomed. Opt.* 14:030502–030503.

8. Mertz, J., and J. Kim. 2010. Scanning light-sheet microscopy in the whole mouse brain with HiLo background rejection. *J. Biomed. Opt.* 15:016027.

9. Mattoussi, H., and J. Cheon, editors. 2009. Inorganic Nanoprobes for Biological Sensing and Imaging. Artech House, Boston, MA Chapt. 4.

10. Muro, E., T. Pons, …, B. Dubertret. 2010. Small and stable sulfobetaine zwitterionic quantum dots for functional live-cell imaging. *J. Am. Chem. Soc.* 132:4556–4557.

11. Winklbauer, R. 1990. Mesodermal cell migration during *Xenopus* gastrulation. *Dev. Biol.* 142:155–168.

12. Nieuwkoop, P. D., and J. Faber. 1994. Normal Table of *Xenopus laevis* (Daudin). Garland Publishing, New York.

13. Smith, W. C., and R. M. Harland. 1991. Injected Xwnt-8 RNA acts early in *Xenopus* embryos to promote formation of a vegetal dorsalizing center. *Cell.* 67:753–765.

14. Neil, M. A. A., R. Juskaitis, and T. Wilson. 1997. Method of obtaining optical sectioning by using structured light in a conventional microscope. *Opt. Lett.* 22:1905–1907.

15. Stokseth, P. A. 1969. Properties of a defocused optical system. *J. Opt. Soc. Am.* 59:1314–1321.